

## Article

# Enhanced Sodium Storage Performance of Few-Layer Graphene-Encapsulated Hard Carbon Fiber Composite Electrodes

Bo Zhu <sup>1</sup>, Tianyi Ji <sup>2</sup> , Qiong Liu <sup>3</sup> and Lixin Li <sup>1,\*</sup> 

<sup>1</sup> School of Innovation and Entrepreneurship, Heilongjiang University of Science & Technology, Harbin 150020, China

<sup>2</sup> School of Materials Science and Engineering, Shaanxi University of Science & Technology, Xi'an 710021, China

<sup>3</sup> Xi'an Herong New Energy Technology Co., Ltd., Xi'an 710018, China; 4325@sust.edu.cn

\* Correspondence: lixin1980@163.com

**Abstract:** Hard carbon anodes are promising for sodium-ion batteries due to their low cost and high reversible capacity. However, the long-term Na<sup>+</sup> (de)intercalating process destroys the structure of the two-phase interface between the electrode and electrolyte, impairing cycling stability. In this paper, a few-layer graphene (FLG)-coated hard carbon fiber composite is constructed. A uniform graphene encapsulation is confirmed by synchrotron small-angle X-ray scattering and transmission electron microscopy technologies. Post-cycling observation reveals FLG participation in forming a hybrid solid electrolyte interphase (SEI). At a proper concentration, the FLG with a small specific surface area and pore size characteristics is well matched in the SEI. The FLG-integrated SEI not only mitigates volume expansion but also enhances ion conductivity through its oxygen-rich functional groups. As a result, the composite structure maintains 98.2% capacity retention after 100 cycles and reaches 164 mAh g<sup>-1</sup> at 1000 mA g<sup>-1</sup>, compared to 97 mAh g<sup>-1</sup> for the pristine hard carbon. This work demonstrates that FLG coating simultaneously stabilizes the interfacial chemistry and improves the ion transport, offering a practical pathway to advance hard carbon anodes for high-performance sodium-ion batteries.

**Keywords:** hard carbon; few-layer graphene; sodium-ion battery; solid electrolyte interface



Academic Editor: Dino Tonti

Received: 13 April 2025

Revised: 7 May 2025

Accepted: 17 May 2025

Published: 21 May 2025

**Citation:** Zhu, B.; Ji, T.; Liu, Q.; Li, L.

Enhanced Sodium Storage

Performance of Few-Layer Graphene-Encapsulated Hard Carbon Fiber

Composite Electrodes. *Batteries* **2025**,

11, 203. <https://doi.org/10.3390/batteries11050203>

**Copyright:** © 2025 by the authors.

Licensee MDPI, Basel, Switzerland.

This article is an open access article distributed under the terms and conditions of the Creative Commons Attribution (CC BY) license

(<https://creativecommons.org/licenses/by/4.0/>).

## 1. Introduction

Sodium-ion batteries (SIBs) have emerged as a promising alternative energy storage technology in the post-lithium-ion era owing to their abundant resource availability, cost-effectiveness, and comparable electrochemical properties [1–3]. Among various anode materials for sodium storage, hard carbon has become the preferred choice due to its wide availability, tunable structure, and superior performance in terms of capacity, rate capability, and initial Coulombic efficiency (ICE) [4–6].

In pursuit of further improving the sodium storage properties of hard carbon, extensive research has focused on modifying its intrinsic structure. For instance, closed pore engineering has been employed to improve the low-potential plateau capacity [7,8], while grain size optimization has been demonstrated to enhance the rate performance [9,10]. Although structural modulation is crucial for achieving theoretically optimal performance, the electrode–electrolyte interfacial properties also play a critical role in determining sodium storage behavior [11–13]. Specifically, interfacial processes such as desolvation kinetics influence rate capability, whereas the composition and stability of the solid electrolyte interphase (SEI) affect the ICE and long-term cycling stability [14–16]. Poor interfacial design can lead to detrimental side reactions, resulting in performance degradation [17].

Interfacial engineering is, therefore, essential for improving cycling stability and suppressing parasitic reactions. Inorganic coatings are a conventional strategy to prevent direct electrode–electrolyte contact by forming a protective barrier, thereby mitigating side reactions [18,19]. However, such coatings do not contribute to sodium storage, inevitably reducing energy density. Carbon-based protective layers can provide additional sodium storage sites while preserving structural integrity. For example, soft carbon coatings have been explored for hard carbon modification [20,21], but their disordered carbon arrangement often leads to non-uniform coverage. Although metal-ion-assisted carbonization can improve graphitization, subsequent metal removal may compromise coating stability [22,23].

This study introduces a few-layer graphene (FLG)-encapsulated hard carbon fiber composite to achieve a compatible interfacial structure. A uniform graphene encapsulation is revealed through synchrotron SAXS and TEM technologies. Post-cycling TEM images reveal FLG participation in forming a hybrid SEI. At a proper concentration, the few-layer graphene with a small specific surface area and pore size characteristics is well matched in the SEI. Under the appropriate concentration, the few-layer graphene is well matched in the SEI and is not easy to exfoliate. Moreover, the disordered stacking morphology after mixing alleviates the volume expansion, which improves the stability of the interfacial structure. Meanwhile, the rate performance is also enhanced due to the oxygen functional groups of the FLG. Based on the compatible coating strategy, the composite structure maintains 98.2% capacity retention after 100 cycles and reaches  $164 \text{ mAh g}^{-1}$  at  $1000 \text{ mA g}^{-1}$ , compared to  $97 \text{ mAh g}^{-1}$  for the pristine hard carbon. This work demonstrates that FLG coating simultaneously stabilizes the interfacial chemistry and improves ion transport kinetics.

## 2. Experiment

### 2.1. Preparation

In this paper, graphene oxide suspension was obtained out of natural graphite using a redox method [24]. Neutral graphene oxide suspension was obtained by centrifuging the above suspension with deionized water at 8000 rpm and collecting the sediment. The graphene oxide suspension was adjusted to  $0.03 \text{ mg mL}^{-1}$  versus  $0.1 \text{ mg mL}^{-1}$ . Paper towels were fully immersed in the above suspension to adsorb graphene oxide flakes on the surface of the paper towels. After natural air-drying, the tissue paper was pre-oxidized at  $250^\circ\text{C}$  in the air for 1 h, after which it was carbonized in an argon atmosphere tube furnace at  $1300^\circ\text{C}$  for 1 h to obtain graphene-coated hard carbon fiber composites with a few layers.

### 2.2. Structural Characterization

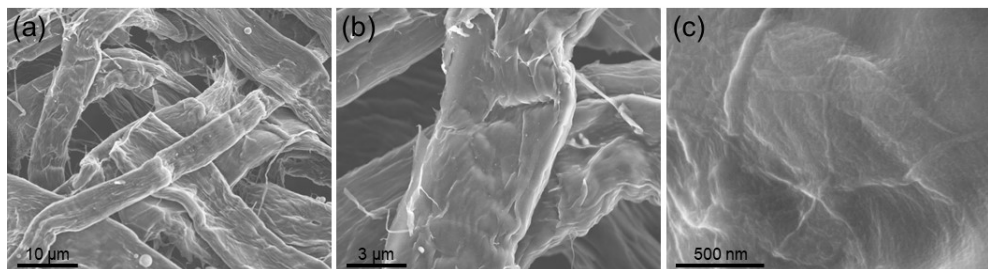
The crystal structure was analyzed by X-ray diffraction (XRD) with a Bruker diffractometer (D8 ADVANCE, Bruker, Bremen, Germany). The molecular structure is characterized by Raman spectroscopy (R) (inVia Reflex device, 532 nm, Renishaw, Gloucester, UK). Transmission electron microscopy (TEM; Tecnai G2 F20 S-TWIN, 200 kV, FEI, Hillsboro, OR, USA) and scanning electron microscopy (SEM; Hitachi S4800, 15 kV, Hitachi, Tokyo, Japan) were performed for microstructural analysis. In order to avoid damage to the interface structure by the electron beam during the photographing process, the position was moved to photograph the edge structure immediately after adjusting the focus. The element and chemical state information were recognized by X-ray photoelectron spectroscopy (XPS; Thermo ESCALAB 250XI, Thermo Fisher, Waltham, MA, USA). The specific surface area and pore size were tested on the BSD-660 analyzer (Beishide Instrument, Beijing, China). Synchrotron SAXS tests were performed at the Beijing synchrotron radiation 1W2A workstation.

### 2.3. Electrochemical Testing

The prepared material was a self-supporting structure, which was cut and used directly as electrode material with an area loading of  $1.5 \text{ mg cm}^{-2}$ . Coin cell (CR2032) assembly was carried out in a glove box ( $\text{O}_2$  and  $\text{H}_2\text{O} < 0.1 \text{ ppm}$ ) with an encapsulation pressure of 70 MPa. Glass fibers (Whatman GF/A) were used as separators and sodium metal foils were used as counter/reference electrodes. The cells used an ether electrolyte (1.0 M  $\text{NaCF}_3\text{SO}_3$  in DIGLYME) with a 70  $\mu\text{L}$  addition. Charge/discharge tests were performed on a Neware test system (2.0–0.01 V vs.  $\text{Na}^+/\text{Na}$ ). Measurements of cyclic voltammetry (CV) and electrochemical impedance spectroscopy (EIS) were carried out on a CHI660D electrochemical analyzer from CH Instruments.

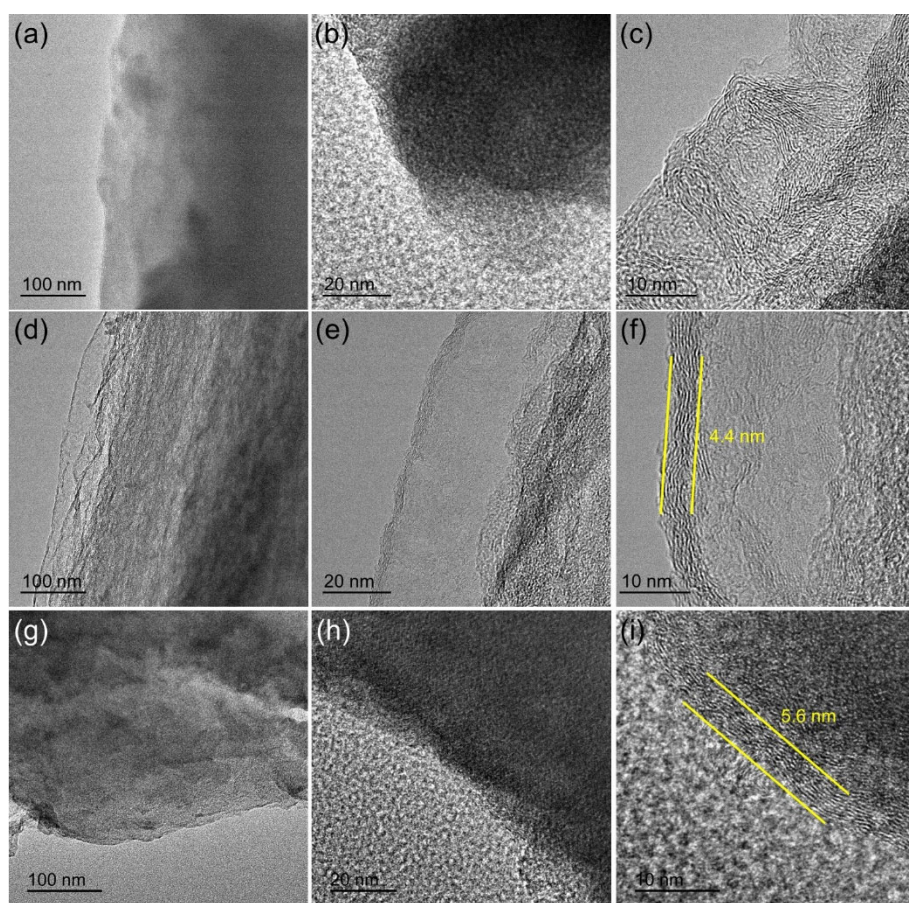
## 3. Results and Discussion

Figure 1a presents a comprehensive SEM analysis of the synthesized hard carbon/graphene composites at progressively increasing magnifications. The hard carbon material exhibits a well-defined fibrous architecture, with individual fibers displaying 5–10  $\mu\text{m}$  diameters. This distinctive one-dimensional morphology, characterized by intertwined carbon fiber networks, provides structural integrity and efficient ion transport pathways in the electrode material. At higher magnifications (Figure 1b,c), the fiber surfaces appear relatively smooth with occasional surface irregularities, suggesting the presence of nanoscale porosity and surface defects inherent to the hard carbon structure. The rGO incorporation was maintained at a deliberately low concentration. Consequently, the ultrathin graphene flakes were not directly resolvable in the SEM images due to their low concentration and the limited contrast between carbonaceous materials. Therefore, TEM further observed the nanostructure of the composite.



**Figure 1.** SEM images of  $0.03 \text{ mg mL}^{-1}$  composite material at different magnifications: (a)  $2000\times$ . (b)  $7000\times$ . (c)  $60,000\times$ .

In Figure 2a–c, the unmodified hard carbon shows a disordered stacking morphology with an amorphous structure at varying magnifications. High-resolution TEM analysis (Figure 2c) reveals an interlayer spacing of 0.41 nm, consistent with the typical turbostratic arrangement of hard carbon materials [6,25]. Following graphene oxide encapsulation, the composite microstructure undergoes significant changes (Figure 2d–f). The hard carbon surface becomes uniformly coated with reduced graphene oxide (rGO) flakes, displaying an ordered layered arrangement with a reduced spacing of 0.37 nm. At a high magnification, the rGO coating is measured to be 4.4 nm thick (Figure 2f), corresponding to approximately six to eight layers, confirming the successful fabrication of an FLG encapsulation. Meanwhile, due to the surface wrinkles of the hard carbon, the TEM images also show that there are voids between the FLG and the hard carbon. To investigate the concentration-dependent effects, a composite with a higher graphene oxide precursor concentration was prepared (Figure 2g–i). While the rGO interlayer spacing remains unchanged at 0.37 nm, the coating thickness increases to 5.6 nm, demonstrating that GO concentration primarily modulates the cladding thickness rather than the structural order of the graphene layers.



**Figure 2.** TEM images at different magnifications: (a–c)  $0 \text{ mg mL}^{-1}$ . (d–f)  $0.03 \text{ mg mL}^{-1}$ . (g–i)  $0.1 \text{ mg mL}^{-1}$ .

X-ray diffraction analysis (Figure 3a) reveals distinct structural differences between the samples, providing critical insights into the crystallographic evolution induced by rGO incorporation. The pristine hard carbon exhibits characteristic amorphous carbon features [26], as evidenced by a broad (002) diffraction peak centered at  $21.7^\circ$  ( $d_{002} = 0.41 \text{ nm}$ ), which is typical for disordered carbon materials with turbostratic stacking of graphene-like layers. This relatively sizeable interlayer spacing suggests the presence of significant structural defects and imperfect stacking arrangements. Upon incorporation of rGO, a remarkable structural transformation occurs, manifested by the (002) peak shifting to higher  $2\theta$  values, ultimately reaching  $24.3^\circ$  for the composites, corresponding to a substantially reduced interlayer spacing of  $0.37 \text{ nm}$ . This systematic peak shift verifies that the crystalline graphene phase affects the composite's overall crystalline structure. The decreased  $d$ -spacing indicates that rGO is a structural template and ordering agent, promoting more regular layer stacking via  $\pi$ - $\pi$  interactions between graphene sheets and the hard carbon matrix.

Raman spectroscopy (Figure 3b) provides complementary and more detailed insight into the structural ordering at the molecular level. The spectra display two prominent first-order features: the disorder-induced D-band ( $\sim 1350 \text{ cm}^{-1}$ ), arising from the breathing modes of sp<sup>2</sup> carbon atoms in rings and reflecting structural defects, and the graphitic G-band ( $\sim 1580 \text{ cm}^{-1}$ ), corresponding to the in-plane vibrational mode of sp<sup>2</sup>-bonded carbon atoms [27–29]. Quantitative analysis reveals progressively decreasing  $I_D/I_G$  ratios (from 1.76 for pristine hard carbon to 1.62 for the composite) with an increasing rGO concentration, demonstrating enhanced structural ordering through graphene incorporation. This trend

indicates a reduction in the defect density and the development of more extended graphitic domains, correlating well with the XRD observations of improved crystallinity.

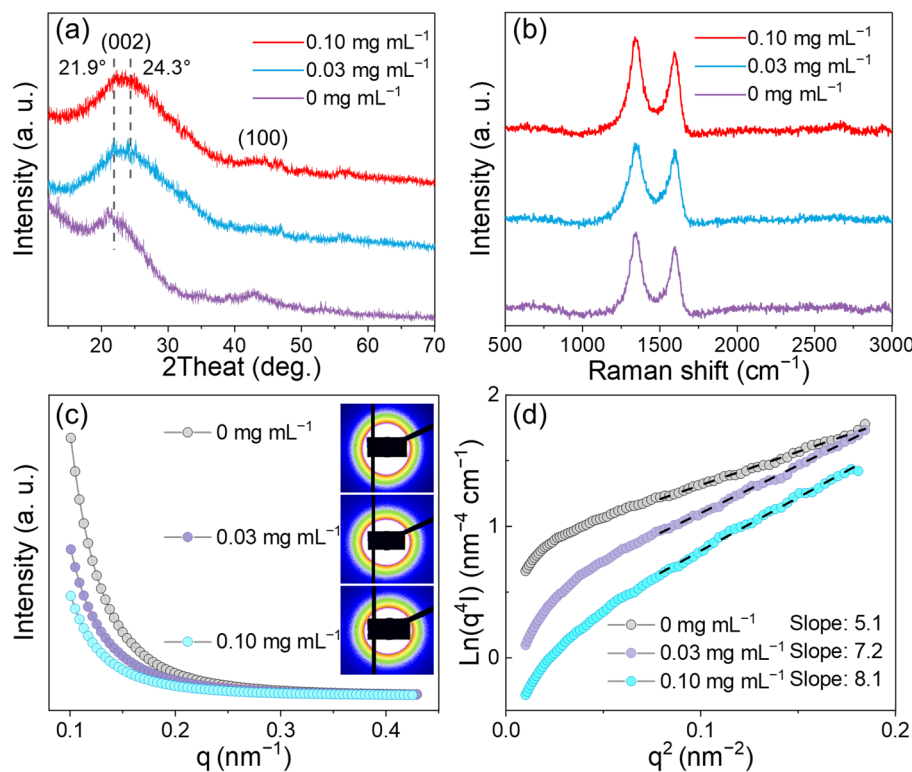


**Figure 3.** Spectral characterization of hard carbon and graphene-encapsulated hard carbon: (a) XRD. (b) Raman. (c) SAXS one-dimensional curves and scattering patterns; (d) Porod curves.

Synchrotron SAXS provides critical insights into the nanoscale morphological evolution induced by graphene coating (Figure 3c). The scattering pattern undergoes a distinct transformation, progressing from an initially elliptical (anisotropic) profile, indicative of oriented, hard carbon fibers with preferential alignment, to a near-circular (isotropic) scattering distribution at high graphene loadings. This transformation indicates that the uniform coating structure of graphene on the whole fiber has been formed. This uniform encapsulation ensures consistent interfacial properties and charge transport pathways throughout the composite.

Further quantitative Porod analysis (Figure 3d) reveals a systematic increase in the slope magnitude in the high- $q$  region with higher graphene concentrations. This enhanced positive deviation from Porod's law signifies a significant transition in the interfacial structure between the hard carbon and graphene phases [30–32]. The observed trend suggests the development of a more defined, smooth boundary with reduced electron density fluctuations, consistent with the formation of a well-organized graphene-hard carbon interface. These spectroscopic and SAXS analyses and TEM observations confirm the successful formation of a stable two-phase interface comprising highly crystalline FLG uniformly coating the low-crystallinity hard carbon matrix.

Galvanostatic charge/discharge analysis demonstrates that the  $0.03 \text{ mg mL}^{-1}$  composite performs optimally, as shown in Figure 4a–c, delivering  $334 \text{ mAh g}^{-1}$  reversible capacity at  $30 \text{ mA g}^{-1}$  and 71.7% ICE. The performance deteriorates at a higher concentration ( $0.1 \text{ mg mL}^{-1}$ ), showing 12% lower capacity and 8% reduced ICE. The ICE values between the optimal composite and the pristine hard carbon were similar, but the capacity of the composite is enhanced compared to the hard carbon. In order to understand the changes

in the ICE and capacity, N<sub>2</sub> adsorption/desorption and XPS analyses were performed on both materials.

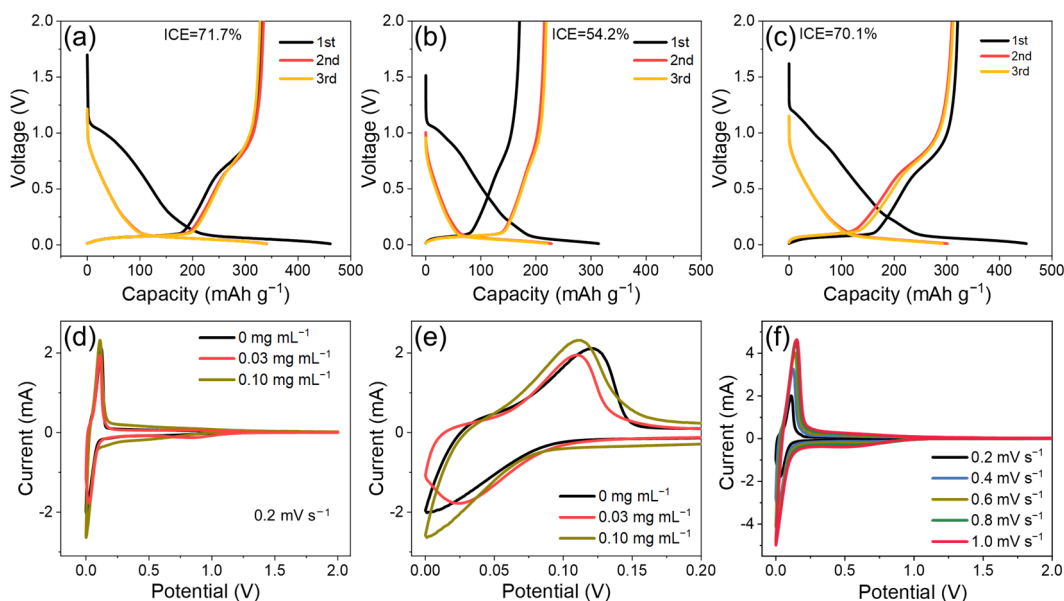


**Figure 4.** Charge–discharge curves: (a)  $0.03 \text{ mg mL}^{-1}$ . (b)  $0.1 \text{ mg mL}^{-1}$ . (c)  $0 \text{ mg mL}^{-1}$ . CV curves: (d,e) different materials in  $0.2 \text{ mV s}^{-1}$ . (f) different scan rates of  $0.03 \text{ mg mL}^{-1}$  sample.

For the ICE, there is no major difference in this metric between coated (71.7%) and pristine hard carbon (70.1%). Instead, the high concentration of graphene had an overall negative effect on the electrochemical performance, such as a sharp decrease in the ICE (54.2%). Since the low-concentration samples and the pristine hard carbon have a similar specific surface area and pore structure (as shown in Supplementary Figure S1), the ion loss during SEI formation is similar. However, excessive concentration of graphene leads to its easy exfoliation from the surface of the hard carbon fibers, resulting in an increase in ion loss. Moreover, the introduction of the FLG brings more oxygen doping to the surface (Supplementary Figure S2), so the capacity is improved by about  $30 \text{ mAh g}^{-1}$  on the basis that the interfacial structure remains stable.

To evaluate the composites' electrochemical properties, CV experiments were carried out. Figure 4d reveals that all samples exhibit characteristic redox peaks associated with Na<sup>+</sup> storage. Notably, the composite with  $0.03 \text{ mg mL}^{-1}$  graphene loading demonstrates significant peak broadening in the low-voltage region (0–0.1 V). In contrast, the pristine hard carbon and high-concentration composites maintain nearly identical reduction peak profiles (Figure 4e). This distinct electrochemical response suggests that at optimal graphene loading ( $0.03 \text{ mg mL}^{-1}$ ), the FLG primarily facilitates interfacial electrochemical processes rather than serving as dominant Na<sup>+</sup> storage sites. The excellent CV curve stability across various scan rates (Figure 4f) further confirms the robustness of the graphene-mediated interfacial reactions.

Figure 5a systematically evaluates the rate capability for different samples, revealing that the composite with  $0.03 \text{ mg mL}^{-1}$  graphene loading achieves optimal electrochemical performance. This optimized material delivers outstanding specific capacities of 279, 248, 220, 194, and  $164 \text{ mAh g}^{-1}$  at progressively increasing current densities from 50 to  $1000 \text{ mA g}^{-1}$ . In striking contrast, the high-concentration composite ( $0.10 \text{ mg mL}^{-1}$ ) exhibits a significantly degraded rate performance, with capacity values approximately 25–35% lower across all tested current densities. The capacity drops and Coulomb efficiency instability at high loadings also indicate the weak bonding state between the surface graphene and the hard carbon fibers. The electrochemical impedance spectra

(Supplementary Figure S3) also indicate that the optimal loading case contributes to a reduction in the charge transfer resistance, while if it is too high it has a negative effect. The cycling stability tests (Figure 5b) further highlight the advantages of the optimized graphene loading. The  $0.03 \text{ mg mL}^{-1}$  composite shows remarkable capacity retention (98.2% after 100 cycles) and stable Coulombic efficiency (99.2% average) when cycled at  $50 \text{ mA g}^{-1}$ . These results show that the FLG coating effectively enhances interfacial stability while maintaining efficient ion transport.

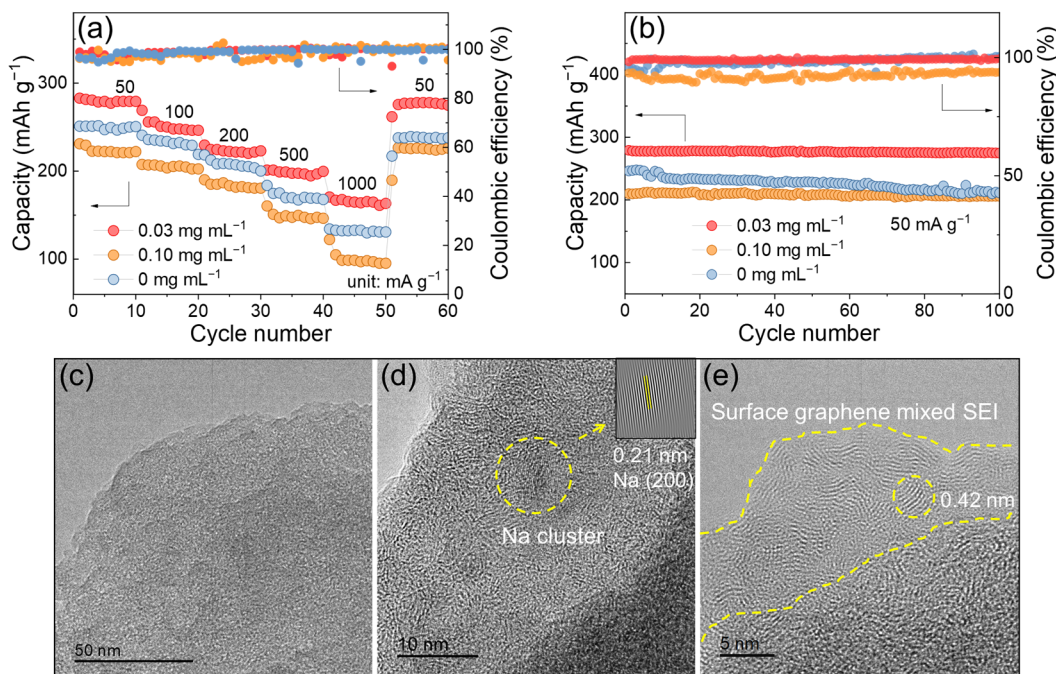


**Figure 5.** Electrochemical testing and microstructure after discharge: (a) Rating; (b) Cycling; (c–e) TEM images of  $0.03 \text{ mg mL}^{-1}$  sample after discharging to  $0.01 \text{ V}$ .

The TEM observation of a  $0.03 \text{ mg mL}^{-1}$  composite sample discharged to  $0.01 \text{ V}$  was carried out to investigate the mechanism of the interfacial structure on enhancing sodium storage performance. As displayed in Figure 5c, the composite maintains its lamellar stacking architecture after discharging. Upon further magnification, a clear elliptical highly crystalline region with a long axis of less than  $10 \text{ nm}$  is shown inside the structure in Figure 5d, which was analyzed to indicate that the lattice fringes in the region belonged to the (200) crystalline plane of sodium metal; this originated from the sodium–metal deposition storage mechanism in the hard carbon material [33,34]. Further magnification of the edge region in the figure shows a transparent solid electrolyte interface layer in Figure 5e, and this interface structure is mixed with a few layers of graphene on the surface, resulting in the rearrangement of graphene on the surface. The thickness of this mixed SEI is roughly  $10\text{--}20 \text{ nm}$ , and the spacing of the graphene layer increases, indicating that  $\text{Na}^+$  undergoes interlayer insertion behavior in it. The above results suggest that the FLG with a small specific surface area and pore size characteristics is well matched in the SEI at a proper concentration. Compared to literature reports [19], the thicker interfacial structure observed with FLG results from the stacking deformation of graphene layers during the SEI formation. Nevertheless, this unique hybrid SEI incorporated with the FLG significantly enhances the interfacial stability to buffer the volume expansion during cycling. Consequently, these synergistic effects lead to remarkable improvements in the composite electrode material’s cycling stability.

Furthermore, related studies have demonstrated that sub-nanoscale structures can facilitate desolvation [35–37]. These atomic-scale regions can catalyze the desolvation of solvated ions, thereby reducing the desolvation energy. Accordingly, the pore size analysis results in Figure S1 show that the pore size of the FLG is smaller in comparison, which, combined with the TEM results after discharge in Figure 5e, suggests that some sub-nanoscale structures exist in the hybrid SEI. Meanwhile, the oxygen-rich functional groups in the FLG help to accelerate ion diffusion [38,39]. Therefore, this FLG-hybridized SEI helps to promote the desolvation and ion diffusion processes, and thus the rate performance is improved. Compared to other coating forms, the FLG-encapsulated structure demonstrates a comprehensive advantage (as shown in Supplementary Table S1), showing the potential application value of this strategy.

#### 4. Conclusions

The integration of FLG with hard carbon fibers results in the formation of a graphene-hybridized SEI during the initial discharge process. This FLG-hybridized SEI has good stability and enhanced ion transport kinetics, attributed to the oxygen-rich functional groups in the FLG and is well matched within the SEI matrix. Hence, the composite anode demonstrates markedly enhanced cycling performance and rate capability relative to unmodified hard carbon. The hybrid structure alleviates the structural degradation induced by prolonged  $\text{Na}^+$  (de)intercalation or volume changes. However, excessive graphene thickness can have overall detrimental effects. At the optimal composition, the composite exhibits 98.2% capacity retention over 100 cycles with 99.2% average Coulombic efficiency. It achieves  $334 \text{ mAh g}^{-1}$  at  $30 \text{ mA g}^{-1}$  and maintains  $164 \text{ mAh g}^{-1}$  at  $1000 \text{ mA g}^{-1}$ , showcasing the potential of the FLG coating strategy for advancing hard carbon material.

**Supplementary Materials:** The following supporting information can be downloaded at: <https://www.mdpi.com/article/10.3390/batteries11050203/s1>. References [40,41] are cited in the Supplementary Materials. Figure S1: Analysis of specific surface area and pore size; Figure S2: XPS analysis; Figure S3: EIS tests for three samples; Table S1: Performance comparison of different coating structures.

**Author Contributions:** Conceptualization, B.Z.; methodology, B.Z. and T.J.; software, Q.L.; validation, Q.L. and L.L.; formal analysis, B.Z. and T.J.; investigation, B.Z. and T.J.; resources, B.Z. and L.L.; data curation, B.Z. and T.J.; writing—original draft preparation, B.Z.; writing—review and editing, B.Z. and L.L.; visualization, T.J.; supervision, L.L.; project administration, L.L.; funding acquisition, Q.L. and L.L. All authors have read and agreed to the published version of the manuscript.

**Funding:** This research was funded by Key Special Projects for the Integration of Two Chains in Shaanxi Province (2024ZG-JBGS-08) and Natural Science Foundation of Heilongjiang Province (LH2023E125).

**Data Availability Statement:** The data that support the findings of this study are available from the corresponding author upon reasonable request.

**Acknowledgments:** The authors appreciate the financial support from Key Special Projects for the Integration of Two Chains in Shaanxi Province (2024ZG-JBGS-08). This work was supported by Beijing synchrotron radiation 1W2A workstation in China.

**Conflicts of Interest:** Author Qiong Liu was employed by the company Xi'an Herong New Energy Technology Co., Ltd. The authors declare no conflict of interest.

## References

1. Zhao, C.; Wang, Q.; Yao, Z.; Wang, J.; Sánchez-Lengeling, B.; Ding, F.; Qi, X.; Lu, Y.; Bai, X.; Li, B.; et al. Rational design of layered oxide materials for sodium-ion batteries. *Science* **2020**, *370*, 708–711. [[CrossRef](#)] [[PubMed](#)]
2. Ge, B.; Deng, J.; Wang, Z.; Liang, Q.; Hu, L.; Ren, X.; Li, R.; Lin, Y.; Li, Y.; Wang, Q.; et al. Aggregate-Dominated Dilute Electrolytes with Low-Temperature-Resistant Ion-Conducting Channels for Highly Reversible Na Plating/Stripping. *Adv. Mater.* **2024**, *36*, 2408161. [[CrossRef](#)]
3. Li, Y.; Liu, X.; Ji, T.; Zhang, M.; Yan, X.; Yao, M.; Sheng, D.; Li, S.; Ren, P.; Shen, Z. Potassium ion doped manganese oxide nanoscrolls enhanced the performance of aqueous zinc-ion batteries. *Chin. Chem. Lett.* **2025**, *36*, 109551. [[CrossRef](#)]
4. Reddy, M.A.; Helen, M.; Groß, A.; Fichtner, M.; Euchner, H. Insight into Sodium Insertion and the Storage Mechanism in Hard Carbon. *ACS Energy Lett.* **2018**, *3*, 2851–2857. [[CrossRef](#)]
5. Iglesias, L.K.; Antonio, E.N.; Martinez, T.D.; Zhang, L.; Zhuo, Z.; Weigand, S.J.; Guo, J.; Toney, M. Revealing the Sodium Storage Mechanisms in Hard Carbon Pores. *Adv. Energy Mater.* **2023**, *13*, 2302171. [[CrossRef](#)]
6. Ji, T.; Liu, X.; Sheng, D.; Li, Y.; Ruan, H.; Guo, H.; Shen, Z.X.; Lai, L. Machine learning-assisted thermomechanical coupling fabrication of hard carbon for sodium-ion batteries. *Energy Storage Mater.* **2024**, *71*, 103563. [[CrossRef](#)]
7. Li, Y.; Vasileiadis, A.; Zhou, Q.; Lu, Y.; Meng, Q.; Li, Y.; Ombrini, P.; Zhao, J.; Chen, Z.; Niu, Y.; et al. Origin of fast charging in hard carbon anodes. *Nat. Energy* **2024**, *9*, 134–142. [[CrossRef](#)]
8. He, X.; Lai, W.; Liang, Y.; Zhao, J.-H.; Yang, Z.; Peng, J.; Liu, X.-H.; Wang, Y.-X.; Qiao, Y.; Li, L.; et al. Achieving All-Plateau and High-Capacity Sodium Insertion in Topological Graphitized Carbon. *Adv. Mater.* **2023**, *35*, 2302613. [[CrossRef](#)]
9. Yang, Y.; Wu, C.; He, X.; Zhao, J.; Yang, Z.; Li, L.; Wu, X.; Li, L.; Chou, S. Boosting the Development of Hard Carbon for Sodium-Ion Batteries: Strategies to Optimize the Initial Coulombic Efficiency. *Adv. Funct. Mater.* **2023**, *34*, 2302277. [[CrossRef](#)]
10. Ji, T.; Liu, X.; Wang, T.; Shi, Y.; Sheng, D.; Hao, X.; He, C.; Shen, Z. Commercial Carbon Fibers as Host for Sodium Deposition to Achieve High Volumetric Capacity. *Adv. Funct. Mater.* **2024**, *34*, 2408880. [[CrossRef](#)]
11. Li, W.; Guo, X.; Song, K.; Chen, J.; Zhang, J.; Tang, G.; Liu, C.; Chen, W.; Shen, C. Binder-Induced Ultrathin SEI for Defect-Passivated Hard Carbon Enables Highly Reversible Sodium-Ion Storage. *Adv. Energy Mater.* **2023**, *13*, 2300648. [[CrossRef](#)]
12. Lu, Z.; Geng, C.; Yang, H.; He, P.; Wu, S.; Yang, Q.; Zhou, H. Step-by-step desolvation enables high-rate and ultra-stable sodium storage in hard carbon anodes. *Proc. Natl. Acad. Sci. USA* **2022**, *119*, e2210203119. [[CrossRef](#)]
13. Li, M.; Wang, C.; Chen, Z.; Xu, K.; Lu, J. New Concepts in Electrolytes. *Chem. Rev.* **2020**, *120*, 6783–6819. [[CrossRef](#)] [[PubMed](#)]
14. Liu, Q.; Rao, A.M.; Han, X.; Lu, B. Artificial SEI for Superhigh-Performance K-Graphite Anode. *Adv. Sci.* **2021**, *8*, 2003639. [[CrossRef](#)]
15. Surace, Y.; Leanza, D.; Mirolo, M.; Kondracki, Ł.; Vaz, C.; El Kazzi, M.; Novák, P.; Trabesinger, S. Evidence for stepwise formation of solid electrolyte interphase in a Li-ion battery. *Energy Storage Mater.* **2022**, *44*, 156–167. [[CrossRef](#)]
16. Yan, C.; Li, H.; Chen, X.; Zhang, X.; Cheng, X.-B.; Xu, R.; Huang, J.; Zhang, Q. Regulating the Inner Helmholtz Plane for Stable Solid Electrolyte Interphase on Lithium Metal Anodes. *J. Am. Chem. Soc.* **2019**, *141*, 9422–9429. [[CrossRef](#)] [[PubMed](#)]
17. Li, Y.; Wu, F.; Li, Y.; Liu, M.; Feng, X.; Bai, Y.; Wu, C. Ether-based electrolytes for sodium ion batteries. *Chem. Soc. Rev.* **2022**, *51*, 4484–4536. [[CrossRef](#)]
18. Yang, Y.; Zhu, J.; Wang, P.; Liu, H.; Zeng, W.; Chen, L.; Chen, Z.; Mu, S. NH<sub>2</sub>-MIL-125 (Ti) derived flower-like fine TiO<sub>2</sub> nanoparticles implanted in N-doped porous carbon as an anode with high activity and long cycle life for lithium-ion batteries. *Acta Phys. Chim. Sin.* **2022**, *38*, 2106002.
19. Lu, H.; Chen, X.; Jia, Y.; Chen, H.; Wang, Y.; Ai, X.; Yang, H.; Cao, Y. Engineering Al<sub>2</sub>O<sub>3</sub> atomic layer deposition: Enhanced hard carbon-electrolyte interface towards practical sodium ion batteries. *Nano Energy* **2019**, *64*, 103903. [[CrossRef](#)]
20. Li, Y.; Xu, S.; Wu, X.; Yu, J.; Wang, Y.; Hu, Y.-S.; Li, H.; Chen, L.; Huang, X. Amorphous monodispersed hard carbon micro-spherules derived from biomass as a high performance negative electrode material for sodium-ion batteries. *J. Mater. Chem. A* **2015**, *3*, 71–77. [[CrossRef](#)]
21. Li, Q.; Zhu, Y.; Zhao, P.; Yuan, C.; Chen, M.; Wang, C. Commercial activated carbon as a novel precursor of the amorphous carbon for high-performance sodium-ion batteries anode. *Carbon* **2018**, *129*, 85–94. [[CrossRef](#)]
22. Cheng, D.; Li, Z.; Zhang, M.; Duan, Z.; Wang, J.; Wang, C. Engineering Ultrathin Carbon Layer on Porous Hard Carbon Boosts Sodium Storage with High Initial Coulombic Efficiency. *ACS Nano* **2023**, *17*, 19063–19075. [[CrossRef](#)]
23. Yu, Z.; Xin, S.; You, Y.; Yu, L.; Lin, Y.; Xu, D.; Qiao, C.; Huang, Z.; Yang, N.; Yu, S.; et al. Ion-Catalyzed Synthesis of Microporous Hard Carbon Embedded with Expanded Nanographite for Enhanced Lithium/Sodium Storage. *J. Am. Chem. Soc.* **2016**, *138*, 14915–14922. [[CrossRef](#)]
24. Ji, T.; Liu, X.; Zhang, T.; Shi, Y.; Sheng, D.; Yin, H.; Shen, Z.X.; Chao, D. Potassium Metal Underpotential Deposition in Crystalline Carbon of Potassium—Ion Batteries. *Adv. Energy Mater.* **2024**, *14*, 2401908. [[CrossRef](#)]
25. Chen, D.; Zhang, W.; Luo, K.; Song, Y.; Zhong, Y.; Liu, Y.; Wang, G.; Zhong, B.; Wu, Z.; Guo, X. Hard carbon for sodium storage: Mechanism and optimization strategies toward commercialization. *Energy Environ. Sci.* **2021**, *14*, 2244–2262. [[CrossRef](#)]

26. Dou, X.; Hasa, I.; Saurel, D.; Vaalma, C.; Wu, L.; Buchholz, D.; Bresser, D.; Komaba, S.; Passerini, S. Hard carbons for sodium-ion batteries: Structure, analysis, sustainability, and electrochemistry. *Mater. Today* **2019**, *23*, 87–104. [CrossRef]
27. Xu, Z.; Guo, Z.; Madhu, R.; Xie, F.; Chen, R.; Wang, J.; Tebyetekerwa, M.; Hu, Y.-S.; Titirici, M. Homogenous metallic deposition regulated by defect-rich skeletons for sodium metal batteries. *Energy Environ. Sci.* **2021**, *14*, 6381–6393. [CrossRef]
28. Bommier, C.; Surta, T.W.; Dolgos, M.; Ji, X. New Mechanistic Insights on Na-Ion Storage in Nongraphitizable Carbon. *Nano Lett.* **2015**, *15*, 5888–5892. [CrossRef] [PubMed]
29. Novko, D.; Zhang, Q.; Kagazchi, P. Nonadiabatic Effects in Raman Spectra of AlCl<sub>4</sub>-graphite Based Batteries. *Phys. Rev. Appl.* **2019**, *12*, 024016. [CrossRef]
30. Li, J.; Yin, J.; Feng, Y.; Liu, Y.; Zhao, H.; Li, Y.; Zhu, C.; Su, B.; Yue, D.; Liu, X. Role of interface between BNNS and LDPE in excellent electrical, thermal and mechanical properties of LDPE/BNNS composites. *J. Mater. Sci. Mater. Electron.* **2019**, *30*, 1531–1540. [CrossRef]
31. Morikawa, Y.; Nishimura, S.; Hashimoto, R.; Ohnuma, M.; Yamada, A. Mechanism of Sodium Storage in Hard Carbon: An X-Ray Scattering Analysis. *Adv. Energy Mater.* **2020**, *10*, 1903176. [CrossRef]
32. Zhang, M.; Liu, X.; Gu, J.; Wang, H.; Liu, H.; Shen, Z. Inspired by nature: Self-fractal cobalt sulfate composite electrode for sodium ion storage. *Chin. Chem. Lett.* **2023**, *34*, 108471. [CrossRef]
33. Chen, X.; Tian, J.; Li, P.; Fang, Y.; Fang, Y.; Liang, X.; Feng, J.; Dong, J.; Ai, X.; Yang, H.; et al. An Overall Understanding of Sodium Storage Behaviors in Hard Carbons by an “Adsorption-Intercalation/Filling” Hybrid Mechanism. *Adv. Energy Mater.* **2022**, *12*, 2200886. [CrossRef]
34. Huang, Y.; Zhong, X.; Hu, X.; Li, Y.; Wang, K.; Tu, H.; Deng, W.; Zou, G.; Hou, H.; Ji, X. Rationally Designing Closed Pore Structure by Carbon Dots to Evoke Sodium Storage Sites of Hard Carbon in Low-Potential Region. *Adv. Funct. Mater.* **2024**, *34*, 2308392. [CrossRef]
35. Chang, Z.; Yang, H.; Qiao, Y.; Zhu, X.; He, P.; Zhou, H. Tailoring the Solvation Sheath of Cations by Constructing Electrode Front-Faces for Rechargeable Batteries. *Adv. Mater.* **2022**, *34*, 2201339. [CrossRef] [PubMed]
36. Deng, J.; Xue, G.; Li, C.; Zhao, S.; Zheng, Y.; He, Y.; Yuan, R.; Wang, K.; Mo, T.; Xiang, Y.; et al. Accelerating Ion Desolvation via Bioinspired Ion Channel Design in Nonconcentrated Aqueous Electrolytes. *J. Am. Chem. Soc.* **2025**, *147*, 5943–5954. [CrossRef]
37. Zhang, X.; Song, T.; He, T.; Ma, Q.; Wu, Z.; Wang, Y.; Xiong, H. Sub-Nanometer Porous Carbon Materials for High-Performance Supercapacitors Using Carbon Dots as Self-templated Pore-Makers. *Adv. Funct. Mater.* **2024**, *35*, 2419219. [CrossRef]
38. Zhou, C.; Li, A.; Cao, B.; Chen, X.; Jia, M.; Song, H. The Non-Ignorable Impact of Surface Oxygen Groups on the Electrochemical Performance of N/O Dual-Doped Carbon Anodes for Sodium Ion Batteries. *J. Electrochem. Soc.* **2018**, *165*, A1447. [CrossRef]
39. Song, Z.; Di, M.; Chen, S.; Bai, Y. Three-dimensional N/O co-doped hard carbon anode enabled superior stabilities for sodium-ion batteries. *Chem. Eng. J.* **2023**, *470*, 144237. [CrossRef]
40. Jialin, G.; Zheng, P. Graphene-coated micro/nanostructure hard carbon with improved electrochemical performance for sodium-ion battery. *Appl. Phys. A* **2021**, *127*, 509. [CrossRef]
41. Gong, Y.; Yu, C.; Li, Y.; Qian, J.; Wu, C.; Bai, Y. Constructing Robust Solid Electrolyte Interface via ZrO<sub>2</sub> Coating Layer for Hard Carbon Anode in Sodium-Ion Batteries. *Batteries* **2022**, *8*, 115. [CrossRef]

**Disclaimer/Publisher’s Note:** The statements, opinions and data contained in all publications are solely those of the individual author(s) and contributor(s) and not of MDPI and/or the editor(s). MDPI and/or the editor(s) disclaim responsibility for any injury to people or property resulting from any ideas, methods, instructions or products referred to in the content.